Dual rotor magnetically geared power split device for hybrid electric vehicles

Petr Chmelicek[1], Stuart Calverley[1], Kais Atallah[2]

[1]Hybrid drives department, Magnomatics ltd, Sheffield, United Kingdom

[2]Department of Electrical and Electronic Engineering, University of Sheffield, Sheffield, United Kingdom

Abstract— The paper presents a theoretical and experimental investigation into a dual rotor magnetically geared power split device for hybrid electric drivetrains. It is shown that the modulation of magnetic field, created by rotor permanent magnets, by an array of ferromagnetic pole pieces results in two dominant space harmonics in the airgap adjacent to the stator. Thus, special attention is given to the design of the stator and the selection of the winding configuration, and the effects of air gap space harmonics on performance of the device are discussed. A full-scale prototype for a mid-sized passenger vehicle is designed, built and tested, and the operation as a power split device is demonstrated and it is shown that efficiencies in excess of 94% can be achieved. Furthermore, torsional vibration attenuation by the proposed device is discussed and experimentally demonstrated on a purpose built test rig.

Index Terms— Magnetic gear, Hybrid drivetrain, Power split

I. Introduction

THE electrification of vehicle drivetrains is an essential step towards reduced energy consumption, improvement of air quality in urban areas and reduction of greenhouse gas emissions. Hybrid electric vehicles will play an important role in meeting the demand for clean and efficient transportation by bridging the gap between current cars with internal combustion engines and future fully electric vehicles.

A hybridized drivetrain combines two or more means of propulsion into a single system, with a typical choice being an internal combustion engine assisted by one or more battery powered electrical machines. The aim of a hybrid drive train is to reduce fuel consumption. Therefore, the strategy employed is to control each component of the drive train, with minimal input from the driver, enabling more efficient vehicle operation.

Over the past two decades, several competing hybrid drivetrain topologies have been developed and commercialized. The most prevalent is the so-called power split hybrid drivetrain which uses two electrical machines combined with an epicyclic gear box to control the flow of power from the internal combustion engine (ICE) to the wheels. In this configuration, ICE speed is independent of the vehicle speed and can be selected in order to meet the power requirements of the vehicle, whilst maximising fuel efficiency. The system acts as a continuously variable transmission system removing the need for a multi speed gear box.
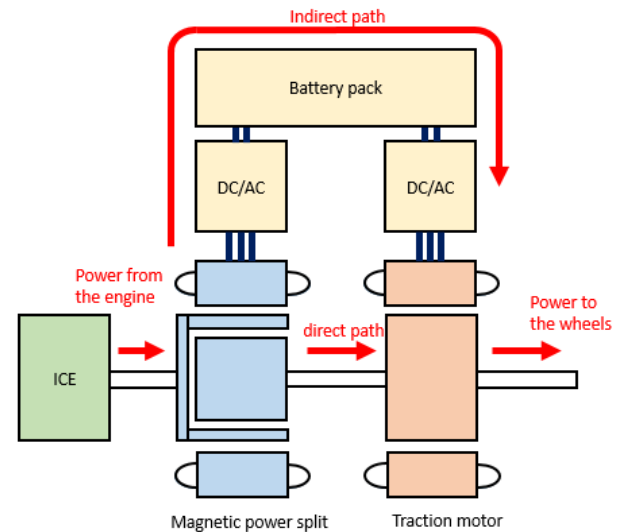

Fig. 1. Hybrid drivetrain utilizing magnetic power split and a traction motor.

The concept of variable magnetic gears, which can be operated as power split devices, was proposed in [1]. A version which consists of a concentric magnetic gear [2] integrated with a brushless permanent magnet (PM) machine was investigated in [3]. It effectively replaces the epicyclic mechanical gear and one of the electrical machines. However, although this would reduce the number of drivetrain components, it is still relatively complex, since it is equipped with three rotors and may require mechanical arrangements with several sets of bearings. The dual rotor device investigated in the paper is an alternative version of the concept described in [1], which omits the second PM rotor, resulting in a reduced amount of PM material and a simpler mechanical layout, with fewer bearings, while maintaining the same functionality. A theoretical study of the space harmonic content and the principle of operation of the dual rotor device was introduced in [4], while an alternative concept where the PM rotor is sandwiched between the pole-piece rotor and the stator was presented in [5]. In [6,7,8], an investigation into the performance of a dual-rotor magnetically geared device is presented. The device is equipped with a distributed winding, however, due to the poor EMF waveform, a step skew is adopted.
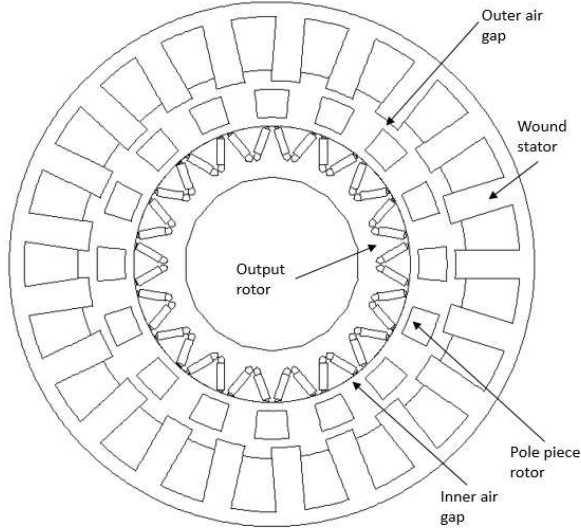
Fig. 2. Cross section of the proposed device.

Therefore, in this paper a theoretical and experimental investigation into the performance of the dual rotor power split topology, Fig. 2, is presented, with special emphasis on the selection of the appropriate combinations of numbers of poles, pole-pieces, and stator slots, in order to achieve the required gear ratios and winding configuration which only couples with the asynchronous harmonic, resulting from the modulation of the magnetic field of the permanent magnet rotor by the pole-piece rotor. It is shown that efficiencies in excess of 94% can be achieved. In addition, possibility of using the device for torsional vibration attenuation is discussed and experimentally demonstrated.

II. PRINCIPLE OF OPERATION

The proposed device is based on the magnetic gearing principle, described in [1], where the magnetic field of a first set of PMs mounted on a rotor is modulated by an array of ferromagnetic pole-pieces, resulting in asynchronous space harmonics in the nonadjacent airgap, the largest of which has the number of pole-pairs:

$$p_c = (n_s - p_m) \tag{1}$$

Where n_s is number of pole pieces and p_m is the number of pole pairs of the permanent magnet rotor.

The asynchronous harmonic interacts with another magnetic field in the nonadjacent airgap, having the same number of pole-pairs and created by a set of windings or PMs, to transmit torque. The speeds of the PM rotor, the pole-piece rotor and magnetic field generated by the array of PMs or the windings are related by:

$$(n_s - p_m)\omega_c = n_s\omega_s - p_m\omega_m \tag{2}$$

$$(n_s - p_m)\theta_c = n_s\theta_s - p_m\theta_m \tag{3}$$

Where ω_m and θ_m are the speed and position of the PM

rotor, respectively, ω_s and θ_s are the speed and position of the pole-piece rotor, respectively. ω_c and θ_c the speed and position of the dominant asynchronous harmonic generated by the interaction of the PMs and the pole-piece rotor, respectively.

Equation (2) is analogous to the following equation which describes speed relations between principal components of a planetary gear set:

$$N_s \, \Omega_s + N_r \, \Omega = (N_s + N_r) \, \Omega_c \tag{4}$$

Where Ω_s, Ω_r, Ω_c is speed of sun gear, ring gear and the carrier respectively, N_s and N_r are number of teeth on sun gear and ring gear. It is apparent from both equations that the functionality of magnetic and mechanical planetary gear is identical.

The asynchronous harmonic interacts with 3-phase stator windings to transmit torque, Fig. 2. Therefore, a fixed ratio magnetic gear can be realised by setting $\omega_c = 0$, while a continuously variable transmission, can be realised by actively varying ω_c. In the version described in [2], the harmonic interacting with stator windings is generated using an array of PMs, which are physically rotated.
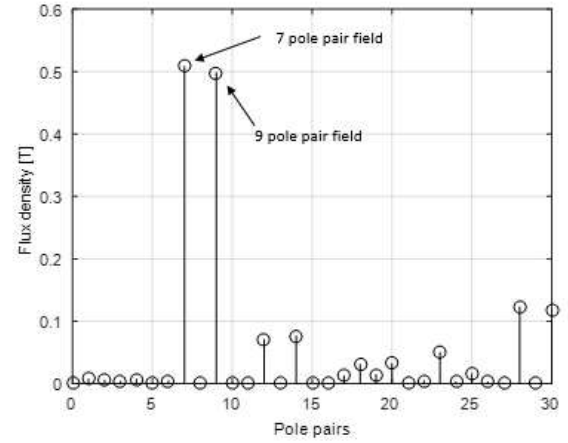

Fig. 3. Spectrum of flux density in the due to the 9 pole-pair rotor PMs in the airgap adjacent to the stator.

The device in Fig. 2 has a 9 pole-pair PM rotor, modulated by 16 ferromagnetic pole pieces. Fig. 3 shows the space harmonic spectrum of the flux density distribution due to the 9 pole-pair PM rotor, in the airgap adjacent to the stator. It can be seen that two dominant space harmonics exist. The first is synchronous and has the same number of pole-pairs as the PM rotor, and the second is asynchronous and has 7 pole-pairs, and interacts with the 3-phase winding on the stator to produce the reaction torque, which enables torque transmission between the PM and the pole-piece rotors. It can also be seen that dominant space harmonics have similar magnitudes; therefore, it is very important to select the winding configuration, which only couples with the asynchronous 7 pole-pair space harmonic.

In normal operation, the dual rotor power split device is equipped with position/speed sensors on each rotor, and the position/speed of the control stator field, which is required for commutation, is derived using equation (3). The feedback

signal is then fed to a conventional three phase automotive inverter connected to the stator windings. Size of the inverter is dictated by the system level design considerations and depends upon required peak and continuous power flow through the electrical path of the hybridized drivetrain.

III. MAGNETIC POWER SPLIT IN AN HEV

In a typical hybrid electric vehicle application, the pole piece rotor is normally coupled directly to the engine whilst the PM rotor serves as the mechanical output. The input power from the engine is split between the output torque acting on the magnet rotor and the stator torque which must be reacted by the stator currents. Torque delivered to the wheels of a vehicle is a sum of torque from the traction motor and from the power split device, as illustrated in Fig. 1.

Fig. 4 shows a diagram illustrating the relationship between speeds of all major components in power split drivetrain of an HEV. Case a) represents a mode of operation where the stator frequency of the power split device is zero, and it operates as fixed ratio magnetic gear, and all the power delivered by the engine is transmitted through the direct mechanical path to the wheels. Case b) represents opposite case where the engine power is converted into electrical power used to charge batteries whilst the vehicle is at stand still. Case c) shows a power splitting operating mode where part of the engine power is converted to electrical power.
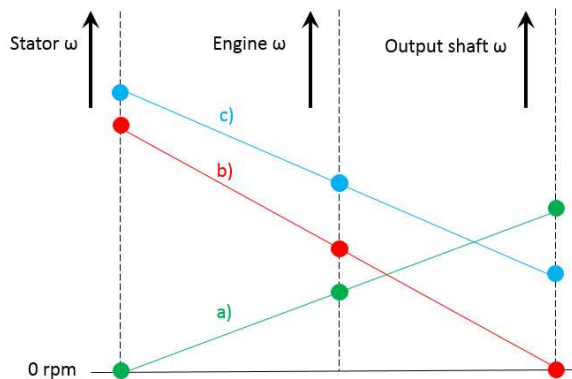

Fig. 4. Example of nomogram of a power split device.

Typically, the machine is operated using maximum torque per Ampere control strategy where the stator currents are in phase with the back EMF generated by the asynchronous harmonic.

Fig. 2 shows a magnetic power split device equipped with an embedded or inset permanent magnet rotor (IPM rotor). These rotors are well known for their so-called inverse saliency, and traditional machines equipped with such rotors exhibit higher inductance in the quadrature axis, and a reluctance torque component. However, due to the large effective airgap, the saliency component of the torque is negligible in the dual rotor device. Fig. 5 shows the variation of the torque with the load angle, where it can be seen that the maximum torque occurs approximately at the load angle of 90º, confirming the small contribution from the saliency torque.

While saliency of the IPM rotor cannot be used to produce reluctance torque, the flux focusing effect of the v-shaped magnet orientation could result in higher amplitude of the control space harmonic compared to an equivalent surface mounted magnet rotor (SPM rotor), as can be seen in Fig. 6 which shows the variation of the amplitude of the control harmonic with the permanent magnet mass. It should be noted that the same air gap of 1mm was assumed for both rotors and thickness of the containment for the SPM rotor was assumed to be significantly smaller than 1mm.
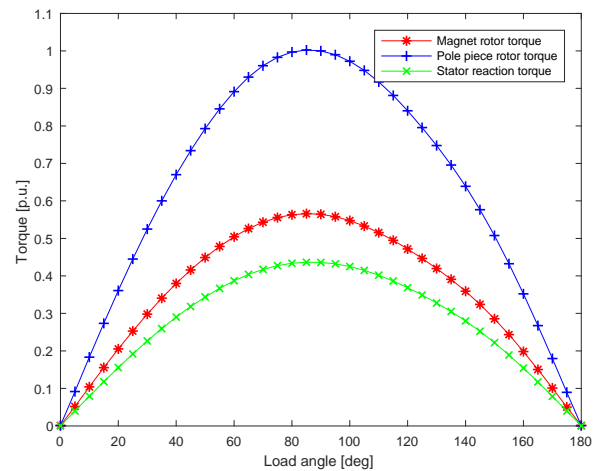

Fig. 5. Variation of torque with load angle at constant slot current density.

Internal combustion engines used in HEV drivetrains, especially those with low cylinder count, produce significant torque ripple. Typical output torque profile produced by a 4 cylinder engine can be seen in Fig. 7. Traditionally, mechanical devices such as dual mass flywheels are employed for torsional vibration attenuation.
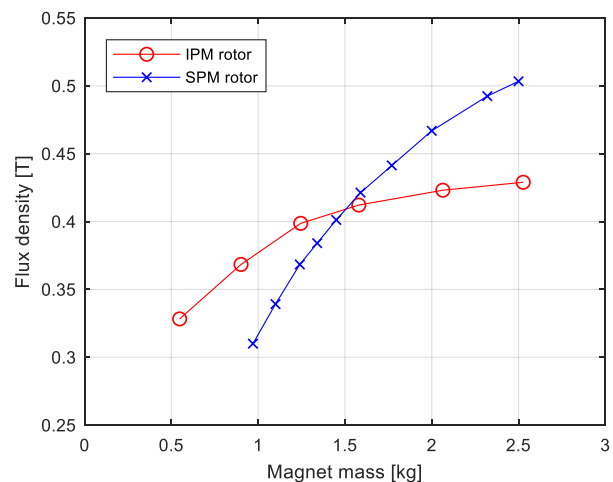

Fig. 6 Amplitude of the useful outer air harmonic as a function of magnet mass for IMP and SPM rotor.

In the proposed device, transmission of torque between the input and the output rotor is governed by the stator field acting

on the asynchronous space harmonic, which is not directly associated with either of the mechanical rotors. Thus, the bandwidth of the controller can be adjusted so that it only reacts to steady state average torque on the input shaft and ignores torque fluctuations associated with piston firing. This leads to theoretically perfect torsional vibration isolation. Detailed discussion of the theoretical principles and dynamic analysis can be found in [9] and in [10]. Additionally, since stator field is essential for torque transmission, loss of stator excitation would result in decoupling of the engine from the rest of the drivetrain.
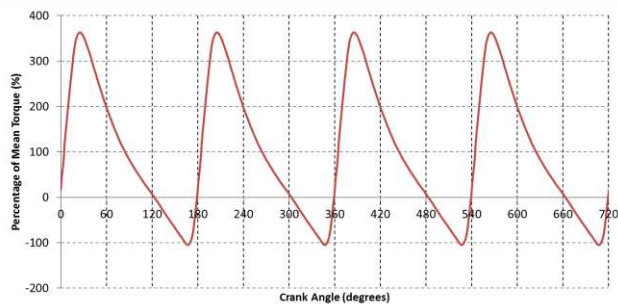

Fig. 7. Typical torque waveform of a 4 cylinder engine as per unit of average torque.

IV. DESIGN IMPLICATIONS OF TWO DOMINANT HARMONICS

In order to ensure that the EMFs induced in the windings are only due to the fluxes associated with the relevant asynchronous space harmonic, special attention must be given to the winding selection. Therefore, ideally the selected winding configuration should have a maximum winding factor for the number of pole-pairs of the relevant asynchronous space harmonic and 0 for the number of pole-pairs of the other dominant synchronous space harmonic.
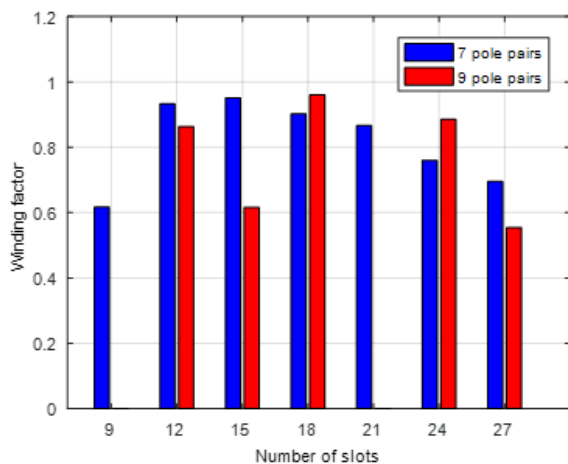

Fig. 8 Winding factors for 7 and 9 pole pairs for different number of stator slots.

For 16 pole-pieces and 9 pole-pair PM rotor, Fig. 8 shows winding factors for 7 and 9 pole pairs for stators with different number of slots, all equipped with double layer concentrated windings. It can be seen that the 21 slot stator provides the

highest winding factor for the relevant 7 pole pair harmonic whilst having no coupling with the 9 pole-pair harmonic, and was selected for the prototype. However, the 9 pole-pair harmonic still induces EMFs of equal magnitudes and 360°/7 degrees out phase in the seven individual coils, A1, A2…A7. Therefore, although the EMFs induced in the coils by the 7 pole-pair harmonic are in phase, they shouldn't be connected in parallel, because this will lead to significant circulating currents causing additional copper losses in the stator winding. Series connection eliminates this problem and is a preferable solution for the particular combination.
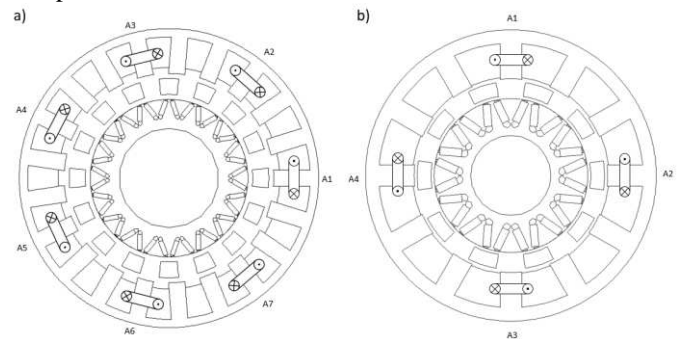

Fig. 9 Cross section of two configurations: a) 21 slot stator, 16 pole pieces and 9 pole pair rotor and b) 12 slot stator, 10 pole pieces and 6 pole pair rotor.

However, there are configurations which allow for parallel connection of the stator coils. An example of such topology is a machine with 6 pole pair magnet rotor and 10 pole pieces, creating asynchronous harmonic with 4 pole pairs. If the stator has 12 slots and is equipped with a double layer concentrated winding there is a natural symmetry between the magnet rotor and the stator windings. Two out of four coils belonging to the same phase have induced EMF of equal magnitude and in phase. Therefore, they can be connected in parallel without the risk of causing significant circulating currents. The resulting winding would have 4 coils per phase and two parallel paths. Cross section of the two discussed configurations with A phase coils can be seen in Fig. 9 while phasor diagrams of EMFs induced in individual coils by the parasitic space harmonic are shown in Fig. 10. Similarly in a machine with 3 pole pair magnet rotor, 5 pole pieces and 6 stator slots where symmetry between double layer winding concentrated winding and magnet rotor exists. Generally, maximum number of parallel paths of concentrated winding depends on symmetry between stator winding and number of poles of the magnet rotor. Even in cases where a parallel connection is possible, attention must be paid to correctly connecting coils which have the same potential at any given time.

A concentrated winding was selected for the prototype as it provides good winding factor for the asynchronous harmonic and also has short end winding. However, distributed windings can be used as long as the requirements described previously are satisfied. Fig. 11 shows winding factors for both dominant space harmonics for different double layer distributed windings. It can be seen that the number of windings which do not couple with the synchronous harmonic is relatively limited.
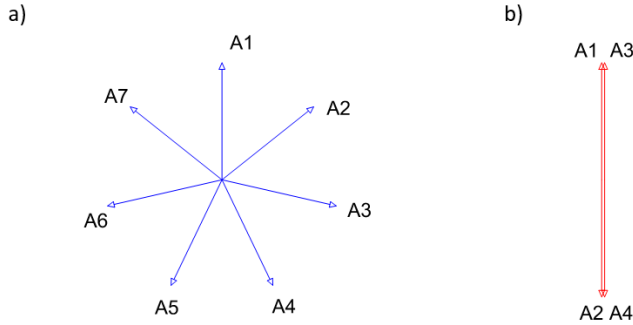
Fig. 10 Phasor diagrams of EMFs induced by dominant parasitic harmonic for a) 21 slot stator, 16 pole pieces and 9 pole pair rotor and b) 12 slot stator, 10 pole pieces and 6 pole pair rotor.
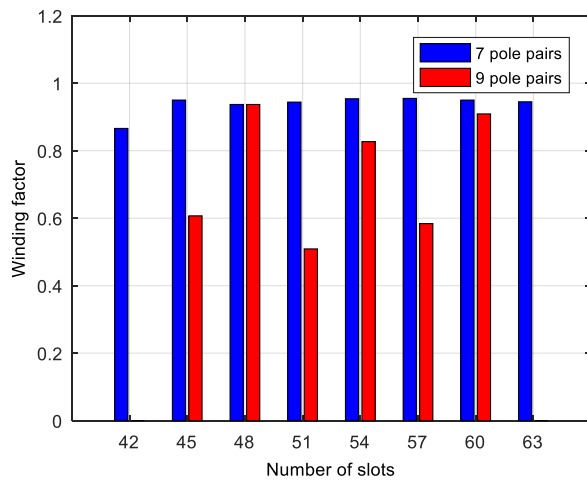

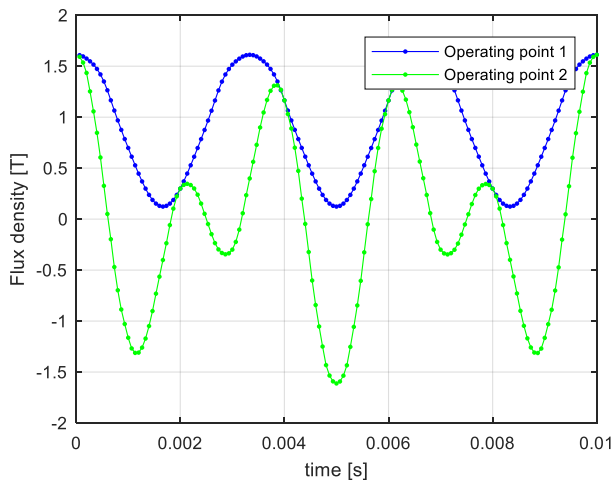Fig. 11 Winding factors for 7 and 9 pole pairs for double layer distributed windings.

Fig. 12 Variation of no load flux density in a stator tooth with time for two operating points of the device.

Another important consideration associated with the 9 pole pair space harmonic is that while it does not contribute to the electromechanical energy conversion, it does produce flux in the stator core, which produces iron losses and may cause

excessive saturation if not taken into consideration at the design stage. This parasitic synchronous harmonic may also increase eddy current losses in the windings. Thus, it is essential to estimate all frequency dependant losses across the operating range of the machine and understand the contribution of each harmonic.

Fig. 12 shows the variation of tooth flux density with time for two no-load operating conditions. Operating point 1 is for input speed of 4500rpm and output speed 0. In this condition, space harmonic due to magnet rotor is stationary while the useful harmonic is rotating at constant speed, hence the sinusoidal variation of flux density with the large DC offset. The operating point 2 represents a situation where both harmonics rotate, and input speed is 3000rpm and the output speed 2000rpm. Frequency of useful 7 pole-pair harmonic can be calculated using equation (1) and for this particular combination of input and output speeds is 500Hz. Frequency of the parasitic 9 pole-pair harmonic associated with the output rotor is 300Hz. Fig 12 shows the variations of tooth flux density for the same two operating points, when the device is operated at peak load. It is clearly apparent that simplified iron loss models, assuming sinusoidal variation of flux density at fundamental stator frequency, would underestimate the iron loss in the stator steel laminations. Advanced time or frequency domain methods, described in [11], must be used for accurate loss computation. It is also worth noting that at most operating points frequency of the parasitic harmonic is not multiple of the stator fundamental frequency.
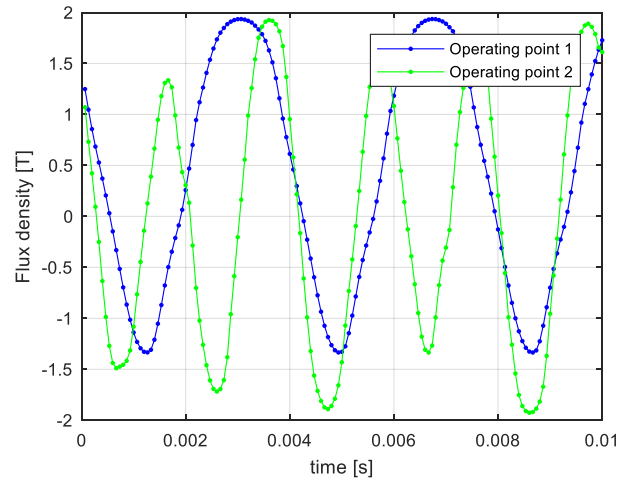

Fig. 13 Variation of rated load flux density in a stator tooth with time for two operating points of the device.

For the proposed device, with parameters in Table 1 and cross section shown in Fig. 2, iron loss was computed using transient 2D FEA analysis. Waveforms of flux density in each element of the finite element mesh were captured and peak values of flux density for each harmonic component were obtained. Peak flux density values together with corresponding frequencies were then used to compute eddy current, hysteresis and excess loss. Total stator iron loss is given as a sum of contributions of individual elements. Specific material constants for M270-35A electrical steel, used for the prototype,

were obtained by curve fitting of iron loss data under different sinusoidal flux density waveforms at different frequencies provided by the steel manufacturer.

In order to obtain total stator power loss, copper loss is also determined. Since stator fundamental frequency could exceed 1000Hz at high differential speeds, AC components of copper loss must be considered. For this purpose a transient 2D FEA model, where each coil consists of individual conductors coupled to an external electrical circuit representing the end-windings, is employed. Detailed explanation of the employed method together with general discussion of AC copper loss can be found in [15]. The model makes it possible to calculate all typical AC copper loss components such as eddy current loss due to skin and proximity effects and loss due to current circulation between parallel strands and coils. The external circuit allows circulating currents to flow between parallel strands via circuit elements representing resistance and inductance of the end-winding portion of each strand. The Contribution of both harmonics to AC copper loss are inherently captured and could be separated by analysing operating points with either zero output speed or zero stator frequency.

Fig. 16 shows the predicted efficiency map of the proposed device at constant rated load, where iron losses in all three principal components and stator copper losses, are considered. Magnet rotor is equipped with NdFeB magnets which are electrically conductive and could be a source of additional eddy current loss, however, for the purpose of the loss analysis, the magnets were assumed to be sufficiently segmented in order to minimize this loss component. Total iron and copper loss maps can be seen in Fig. 14 and Fig. 15 respectively. Efficiency is computed as output over input power but attention must be paid to the direction of electrical power since the stator can operate in either motoring or generating mode. Peak efficiency occurs at peak input speed and, therefore, peak input power. Mechanical losses as well as stray losses in structural components were neglected and will be subject of future research since they are likely to noticeably affect efficiency of the device, especially at higher stator frequency operating conditions.
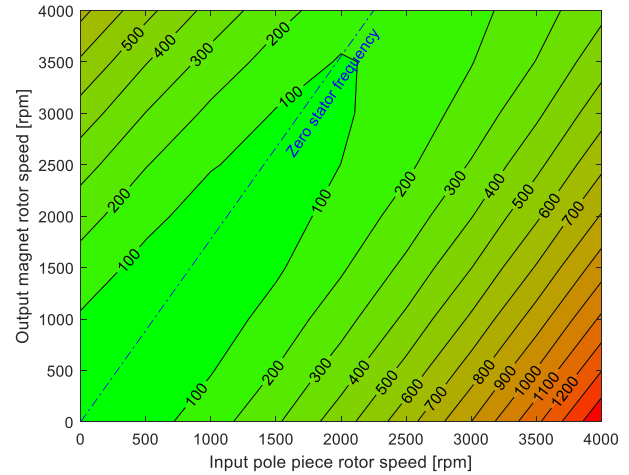

Fig. 14 Total iron loss at rated load in Watts.
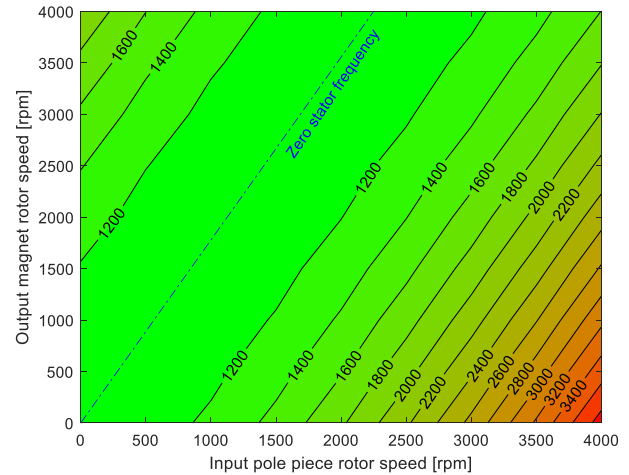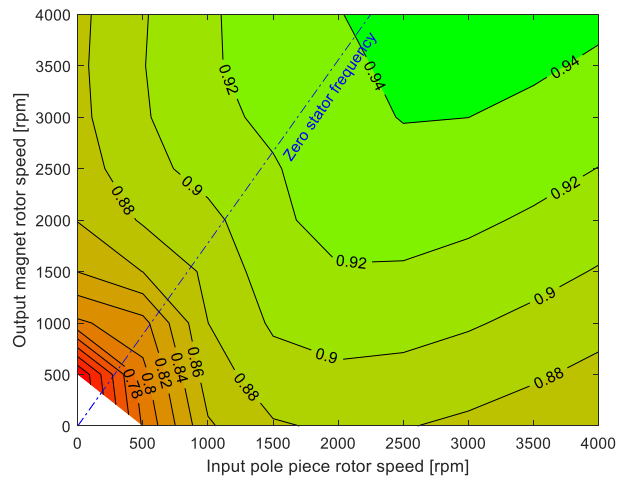

Fig. 15 Copper loss at rated load in Watts.

Fig. 16 Predicted efficiency map for rated load.

V. EXPERIMENTAL VALIDATION

The proposed machine was designed and built in order to demonstrate its operation and assess its performance. The

prototype has a stator outer diameter of 300mm and a 50mm stack length with the cross section shown in Fig. 2. The input shaft is connected to the pole piece rotor, and the PM rotor is coupled to the output shaft. All three principal components of the dual rotor device were made of laminated electrical steel since they are subject of varying magnetic fields. Although semi closed slot stator topology would lead to smaller effective outer air gap, open slot stator was selected because it allows pre-wound coils to be slid onto stator teeth, thus facilitating manufacture and high slot fill factor. Ensuring structural integrity of the pole piece rotor under centrifugal as well as electromagnetic loads is particularly challenging since materials used for its supporting structure must be non-magnetic, so as not to compromise the ability of the pole pieces to modulate the magnetic fields, as well as non-conductive to limit eddy current losses. Table 1 presents main parameters of the prototype machine which is sized for typical ICE of a mid-sized passenger vehicle.

Table 1 Parameters of the prototype machine

Outer diameter [mm]	300
Active length [mm]	50
Peak current [A]	300
Stator pole pairs [-]	7
Pole pieces [-]	16
Magnet rotor pole pairs [-]	9
Stator slots	21
Cooling	Liquid
Winding	Concentrated
Steel grade	M270-35A
Permanent Magnet grade	N48H
DC link voltage [V]	560
Maximum input speed [rpm]	6000
Maximum output speed [rpm]	6000

Fig. 17 shows the prototype on the test rig, whilst Fig. 18 shows schematic layout of the test rig used for the performance evaluation. There are two induction machines connected to two industrial drives, one representing the ICE and the other the mechanical load from the wheels. Control and data acquisition PC is used to collect measured data, such as torques and speeds of both shafts, winding voltages and currents. Input and output shaft of the power split device are equipped with position sensors so that position of the asynchronous harmonic can be estimated and the industrial drive connected to the device can be synchronised with it. With this setup, any combination of input and output speed and load can be tested and the performance evaluated.
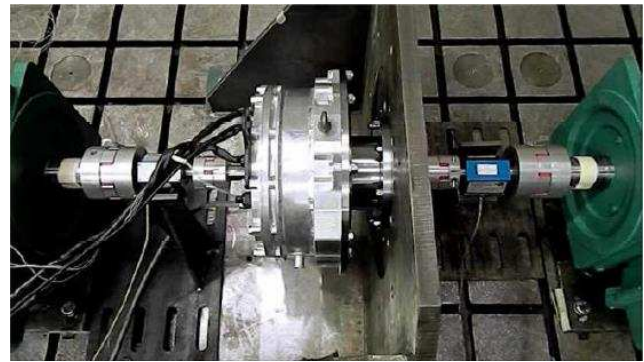

Fig. 17 Prototype on test rig.

Fig. 19 shows the EMF waveforms when the speeds of both rotors is 2000rpm, resulting in a stator electrical frequency of 233Hz, equation (2). It can be seen, there is a good agreement between the predicted using 3D FEA and measured EMFs, and that a low level of harmonic distortion exists, without the need for skewing.

However, predictions using 2D FEA are markedly different due to the relatively short axial length and large outer diameter of the prototype machine combined with large effective air gaps between the three principal components of the device. End-effects of magnetic gears and magnetically geared devices have been comprehensively studied, [13], and the authors concluded that three-dimensional analysis is essential for accurate performance prediction due to the considerable amount of axial leakage, particularly in magnetically geared devices with high ratio of outer diameter to axial length. Furthermore, axial leakage has been identified as a contributor to additional stray loss [14].
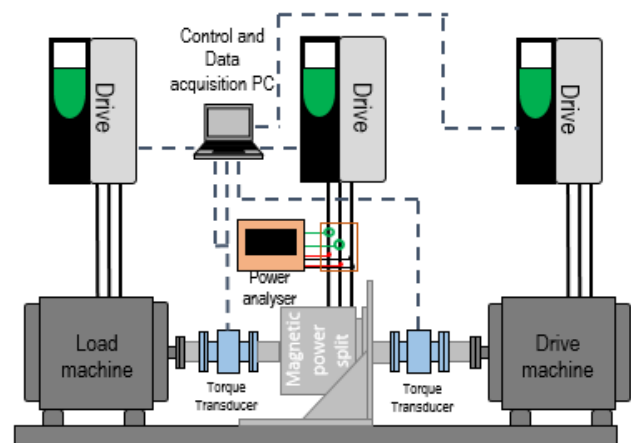

Fig. 18 Test rig schematic.

Fig. 20 shows the variation of the measured and predicted torques on both shafts with the slot current density, when the machine is operated so that the phase EMF is in phase with stator current. It can be seen that due to the saturation of the magnetic circuit, the characteristic is relatively non-linear. It is worth noting that although the peak transmittable torque of the 3 rotor version [3] is limited by the design of the magnetic gear

element, the dual rotor version can be overloaded for short periods of time by increasing the electrical loading of the stator. In addition, it can be seen in Fig. 20 that the difference between measured and 2D FEA predicted torque increases with load, suggesting that the axial leakage is exacerbated by the saturation of the magnetic circuit. Depending on stator load, the difference can be up to 25 percent and may limit the overload capability of the machine.

Fig. 21 shows the variation of the output mechanical and control electrical power with control speed at constant input speed and torque. It can be seen that the input mechanical power is split between mechanical and electrical outputs with a split ratio controlled by the control speed. Fig. 22 shows the efficiency at constant rated stator current and variable input and output speeds, where efficiencies in excess of 94% can be achieved. Efficiency for full range of input and output speeds was not measured due to limited maximal fundamental frequency of the industrial drives used on the test rig, hence the missing data in the bottom right hand corner of the measured efficiency maps. The highest efficiency is achieved with low differential speed between the input and the output shaft, when the stator frequency approaches zero. It is apparent that the measured and predicted peak efficiency is similar. However, at high differential speeds there is notable discrepancy suggesting that loss mechanisms, in particular those associated with the axial stray fields, which were not considered during the efficiency analysis may be significant and will require further investigation. The effect of stator frequency on efficiency is much more pronounced in the measured data. Looking at the line of zero stator frequency, it is apparent that the area of highest efficiency coincides with it.
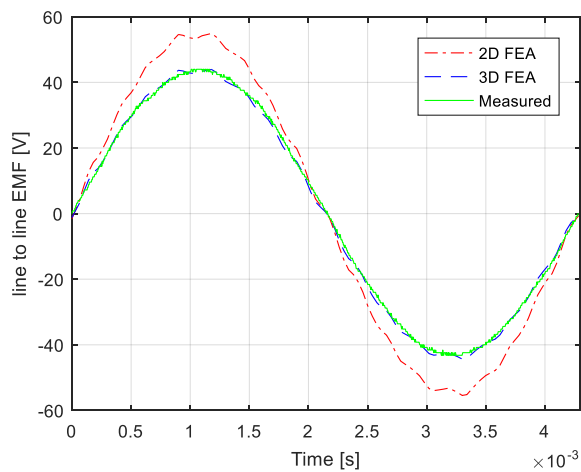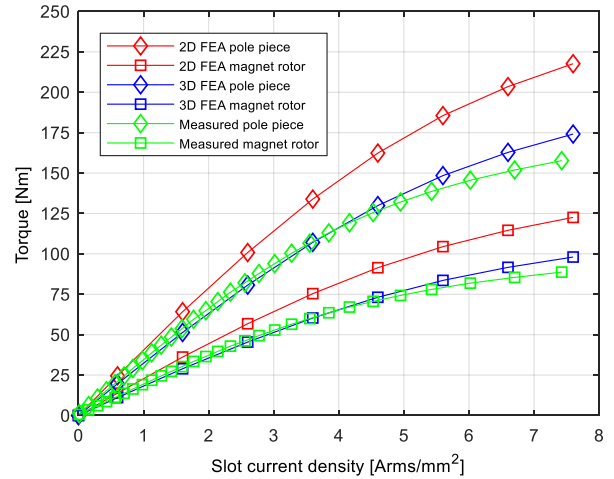
rise in all three phases is achieved.

Fig. 20 Predicted and measured torque as a function of slot current density for both rotors.
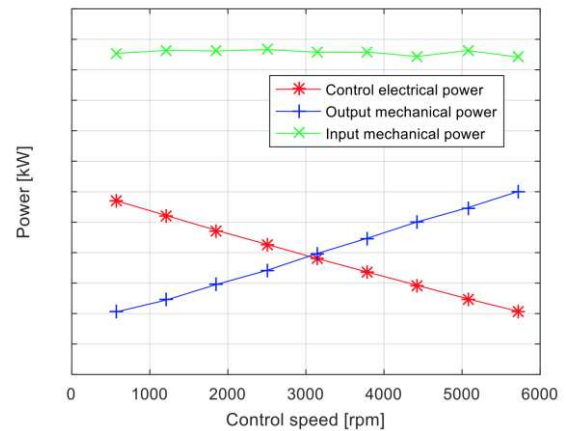
Fig. 21 Measured input, output and control power vs control speed at constant 2500rpm input speed.

Fig. 19 Predicted and measured EMF at 2000rpm input and output speed.
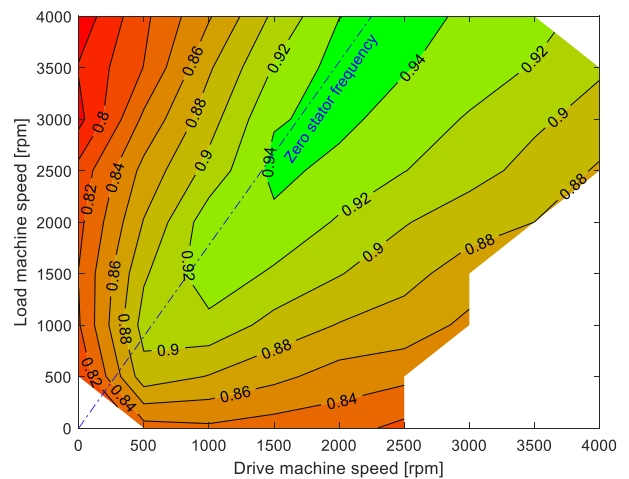
Fig. 22 Measured efficiency map at rated load.

While operation at zero stator frequency is possible and results in the highest efficiency of the device, it could lead to uneven distribution of copper loss among stator phases. However, during a normal operation of the hybrid drivetrain, the device is unlikely to operate at zero stator frequency for significant amount of time. Additionally, the drivetrain of the vehicle can be controlled in such a way that even temperature

Fig. 23 Measured efficiency map at half the rated load.

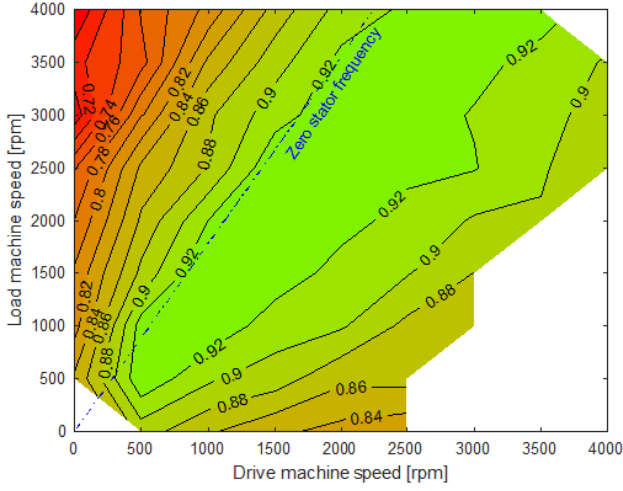Fig. 23 shows the measured efficiency map at half the rated load. It is apparent that while the peak efficiency at half rated load is smaller, the area of constant efficiency is larger.

VI. VIBRATION ATTENUATION

The dynamic equations governing the operation of the device are given by:

$$J_p \frac{d^2\theta_p}{dt^2} = T_i - \frac{n_s}{p_c} T_e \qquad (4)$$

$$J_m \frac{d^2\theta_m}{dt^2} = \frac{p_m}{p_c} T_e - T_l \qquad (5)$$

Where J_p and θ_p are the inertia and the position of the lumped inertia of pole-piece rotor, and other rigidly connected rotors, respectively. J_m and θ_m are the inertia and the position of the PM rotor, respectively. T_i and T_l are the input and load torques, respectively, and T_e is the electromagnetic reaction torque produced by the stator windings. Therefore, torque transmission dynamics are governed by the dynamics of the stator windings and their supply. In a hybrid vehicle application, for a given engine power output, the engine torque and speed are selected to correspond to the highest efficiency. However, while the torque demand is directly sent to the engine, the speed demand is sent to the device which controls the speed of the engine. Hence, the bandwidth of the speed controller is adjusted in order to reduce/eliminate response to the engine ripple frequencies, making the system effectively behave like a filter. This is different to active engine ripple cancellation, which would require the system dynamics to include engine ripple frequencies, in order to actively reduce their effects.

In order to demonstrate this feature, a cam system was added to the test rig shown in Fig. 17 for the purpose of introducing torsional vibration to the input shaft. The two lobe cam system,

Fig. 24, was placed between the drive machine, representing an internal combustion engine, and the input shaft of the dual rotor device. The Input and output torque waveforms are measured using two torque transducers connected to a LabVIEW based data acquisition system. Fig. 25 shows a picture of the physical arrangement.
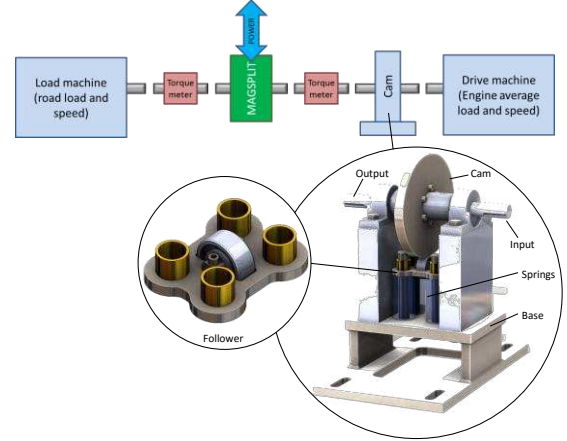

Fig. 24 Schematic of vibration test rig

Fig. 25 Photo of vibration test rig

During the testing, the dual rotor device is operated in torque control mode at constant input speed of 3000rpm imposed by the drive machine. The bandwidth of the current current/torque controller is adjusted to reduce the transmitted ripple introduced by the cam. For an average input torque of 104Nm, Fig. 26 shows the variation the input and output torques with time. It can be seen that the cam introduces a ripple with an amplitude more than 400% of the average torque. However, the measured output torque shows negligible levels of ripple and as expected has an average value of 62Nm, based on the value of input torque and intrinsic gear ratio of the device.

The harmonic spectrum of both the input and output torque waveforms can be seen in Fig. 27. It is apparent that while the spectrum of the input torque is rich in harmonic components, they do not propagate to the output rotor and the rest of the drivetrain. This result is particularly significant given that the vibration attenuation is achieved without introducing a source of power loss to the system.
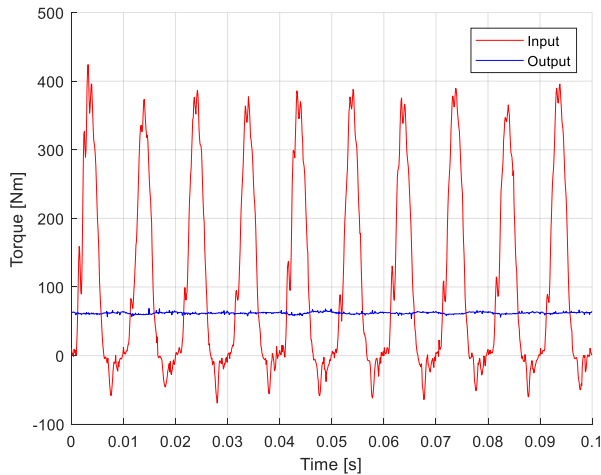
Fig. 26. Variation of measured torques at input and output of the dual rotor device
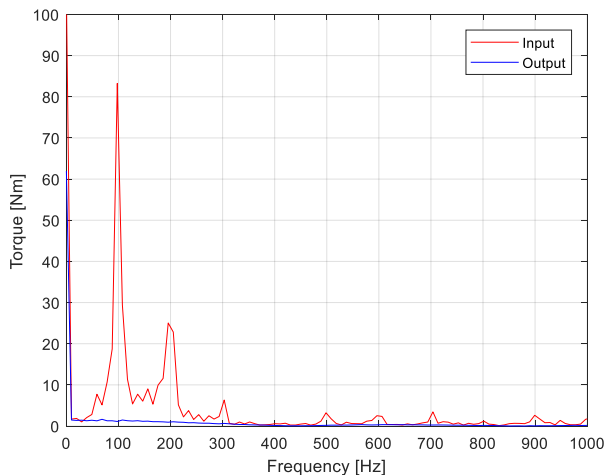

Fig. 27. Frequency spectrum of measured input and output torques

VII. CONCLUSION

Modulation of the magnetic fields produced by the rotor permanent magnets results in two large space harmonics, it is therefore essential to pay special attention to the design of the stator and the selection of the appropriate winding, which only couples with the asynchronous space harmonic. Winding factors for both dominant space harmonics are evaluated for a range of distributed and concentrated windings and it is shown that windings which only couple with the asynchronous harmonic exist.

Furthermore, end effects and axial flux leakage can be significant and 3D FEA is more appropriate in the design and analysis of the dual rotor power split device, especially for devices with short active length. It is shown that the difference between measured and 2D FEA predicted torque can exceed 25% at high loads, particularly when the saturation occurs.

A prototype machine equipped with a double layer concentrated winding was built and tested. With appropriately selected windings, the measured EMF exhibits negligible harmonic distortion, without the need for skewing. Measurements on the prototype have shown that efficiencies in

excess of 94% can be achieved. Predicted efficiencies, where 2D FEA is employed and only iron and copper losses are considered exhibit notable discrepancies with measured results at high differential speeds. Hence, losses in due to the axial fluxes should be considered.

Ability of the dual rotor power split device to filter torsional vibration of the input shaft was discussed and practically demonstrated on a test rig. A cam system coupled to an electrical machine was used to introduce ripple to the input shaft of the device. It can be shown that together with the appropriate control scheme, the proposed device effectively attenuates the ripple from the prime-mover without introducing a source of power loss to the system.

REFERENCES

[1] J. Rens, K. Atallah, "Variable magnetic gears", Patent US9,013081 B2, Apr. 21, 2015.
[2] K. Atallah and D. Howe, "A Novel High-Performance Magnetic Gear", IEEE Transactions on Magnetics, Vol 37, No. 4, July 2001.
[3] K. Atallah, J Wang, S. D. Calverley and S. Duggan, "Design and Operation of a Magnetic Continuously Variable Transmission", IEEE Transaction on Industry Applications, Vol. 48, No. 4, July/August 2012
[4] A. Zaini, N. Niguchi, K. Hirata, "Continously Variable Speed Magnetic Gear", The Japan Society Applied Electromagnetics and Mechanics, 14 March 2012.
[5] M. Fukuoka, K. Nakamura, H. Kato, O. Ichinokura, "A Novel Flux-Modulated Type Dual-Axis Motor for Hybrid Electric Vehicles", IEEE Transactions on Magnetics, Vol. 50, NO. 11, November 2014.
[6] Le Sun, Ming Chen, Hongyun Jia, "Analysis of a Novel Magnetic-Geared Dual-Rotor Motor With Complementary Structure", IEEE Transactions on Industrial Electronics, Vol. 62, No. 11, November 2015.
[7] Le Sun, Ming Chen, Jiawen Zhang, Lihua Song, "Analysis and Control of Complementary Magnetic-Geared Dual-Rotor Motor", IEEE Transactions on Industrial Electronics, Vol.63, No 11, November 2016.
[8] Le Sun, Ming Chen, Jiawen Zhang, Lihua Song,"Motion Control and Performance Evaluation of a Magnetic-Geared Dual-Rotor Motor in Hybrid Powertrain", IEEE Transactions on Industrial Electronics, Vol.64, No 11, March 2017.
[9] Calverley S. D., Birchall, J. G., Black, D.,"High Bandwidth Drivetrain Vibration Attenuation Using Electromagnetic Powersplit Transmission",
[10] Calverley S. D., Birchall, J. G., Black, D.,"Analysis and Verification of Torsional Vibration Attenuation in Automotive Powertrains Using Electromagnetic Powersplit Transmission", EVS29 Symposium, Montreal, Quebec, Canada, June 19-22,2016
[11] D. Kowal, P. Sergeant, L. Dupre, H. Karmaker,"Comparison of Frequency and Time-Domain Iron and Magnet Loss Modeling Including PWM Harmonics in a PMSG for a Wind Energy Application", IEEE Transactions on Energy Conversion, Vol. 30, No. 2, June 2015
[12] P. Chmelicek, S. Calverley, R.S. Dragan, K. Atallah, "Dual rotor magnetically geared power split device for hybrid electric vehicles, " 2017 IEEE International Electric Machines and Drives Conference (IEMDC), Miami, FL, 2017, pp. 1-6.
[13] S. Gerber, R-J. Wang, "Analysis of the End-effects in Magnetic Gears and Magnetically Geared Machines", 2014 International Conference on Electrical Machines (ICEM), 2-5 Sept. 2014
[14] T.V. Frandsen, P.O. Rasmussen, "Practical Investigation of End Effect Losses in a Motor Integrated Permanent Magnet Gear", 2015 IEEE Energy Conversion Congress and Exposition (ECCE), 20-24 Sept. 2015
[15] M. Popescu, D. G. Dorrell, "Skin effect and Proximity Losses in High Speed Brushless Permanent Magnet Motors", 2013 IEEE Energy Conversion Congress and Exposition, Denver, CO, 2013, pp. 3520-3527.